Fully adaptive FEM based fluorescence optical tomography from time-dependent measurements with area illumination and detection

Amit Joshi[a)]
Division of Molecular Imaging, Department of Radiology, Baylor College of Medicine, Houston, Texas 77030

Wolfgang Bangerth
Department of Mathematics, Texas A & M University, College Station, Texas 77840

Kildong Hwang, John C. Rasmussen, and Eva M. Sevick-Muraca
Division of molecular Imaging, Department of Radiology, Baylor College of medicine, Houston, Texas 77030

(Received 10 October 2005; revised 28 February 2006; accepted for publication 2 March 2006; published 21 April 2006)

Using an area-illumination and area-detection scheme, we acquire fluorescence frequency domain measurements from a tissue phantom with an embedded fluorescent target and obtain tomographic reconstructions of the interior fluorescence absorption map with an adaptive finite element based scheme. The tissue phantom consisted of a clear acrylic cubic box (512 ml) filled with 1% Liposyn solution, while the fluorescent targets were 5 mm diameter glass bulbs filled with 1 μM Indocyanine Green dye solution in 1% Liposyn. Frequency domain area illumination and detection employed a planar excitation source using an expanded intensity modulated (100 MHz) 785 nm diode laser light and a gain modulated image intensified charge coupled device camera, respectively. The excitation pattern was characterized by isolating the singly scattered component with cross polarizers and was input into a dual adaptive finite element-based scheme for three dimensional reconstructions of fluorescent targets embedded beneath the phantom surface. Adaptive mesh refinement techniques allowed efficient simulation of the incident excitation light and the reconstruction of fluorescent targets buried at the depths of 1 and 2 cm. The results demonstrate the first clinically relevant noncontact fluorescence tomography with adaptive finite element methods. © *2006 American Association of Physicists in Medicine*. [DOI: 10.1118/1.2190330]

I. INTRODUCTION

Fluorescence enhanced optical tomography is one active area in molecular imaging research. In the past, fluorescence tomography schemes have been proposed for preclinical small animal imaging applications[1] as well as for the clinical imaging of large tissue volumes.[2–15] Typical fluorescence optical tomography schemes employ iterative image reconstruction techniques to determine the fluorescence yield or lifetime map in the tissue from boundary fluorescence measurements. A successful clinically relevant fluorescence tomography system will have the following attributes: (i) rapid data acquisition to minimize patient movement and discomfort, (ii) accurate and computationally efficient modeling of light propagation in large tissue volumes, and (iii) a robust image reconstruction strategy to handle the ill posedness introduced by the diffuse propagation of photons in tissue and the scarcity of data.

Early fluorescence tomography schemes employed point-illumination and point-detection strategies with fiber optics.[13,16] While these strategies can sample the tissue volume from multiple sides, the acquired data sets are sparse owing to the limited number of fiber optics and the slow data acquisition rates. Ntziachristos *et al.*[17] and Godavarty *et al.*[15] employed a hybrid strategy to improve the data acquisition rate of the point illumination and collection schemes by imaging multiple detector fibers with a charge coupled device (CCD) camera. Even with these improvements point illumination and detection schemes might fail in large tissue volumes if sufficient excitation light is not delivered to the target fluorophore, which can happen if the fiber optic sources do not sample the tissue boundary in a sufficiently dense manner. In contrast, area illumination can deliver excitation light over large tissue volumes and thus acquire a dense set of fluorescence measurements rapidly. Further, area illumination and area detection fluorescence measurements do not require physical contact with the imaged entity, making them attractive for clinical applications such as sentinel lymph node imaging to track breast cancer and melanoma as well as for intraoperative use. On the other hand, the challenges in fluorescence tomography with area-illumination and area-detection measurements include: (i) developing measurement schemes to acquire high silicon based negative resist fluorescence measurements rapidly over a large area, (ii) modeling the propagation of light in the tissue that results from a nonuniformly expanded excitation light source incident on the tissue surface, and (iii) managing the ill posedness of the tomography problem stemming from the fact that only a single reflectance measurement is available for image reconstruction.

Recently, Roy and co-workers[14] demonstrated fluorescence yield reconstructions from frequency domain area illumination and detection measurements made on a tissue phantom with an embedded fluorescence target. Their approach required a carefully designed finite element scheme to model the expanded laser excitation source to recover a 1 cm^3 fluorescence target at 1 cm depth. The image reconstruction problem was solved with over 30 000 unknowns, requiring advanced optimization and regularization techniques to maintain stability and accuracy of the solution.

In contrast, the scheme we describe in this article significantly reduces the computational complexity by using automatically adapted meshes. We previously reported this novel fluorescence tomography algorithm employing dual adaptive finite element meshes for area-illumination and area-detection measurement schemes,[18] wherein separate finite element meshes were employed for modeling light propagation in tissue and for describing the unknown fluorescence yield map. Both meshes are adapted independently and automatically. Hence, the spatial distribution of incident excitation light can be modeled accurately and high resolution fluorescence images can be obtained with minimum computational expenditure. As described here, we are able to reduce the total number of unknowns by at least one order of magnitude through this approach. This not only benefits the computational efforts, but at the same time allows for higher resolution in areas where there is variation (e.g., in the vicinity of targets) while keeping the mesh coarse everywhere else. The use of adaptive meshes therefore also reduces the ill conditioning of the problem and helps in finding stable and accurate reconstructions.

In this work we present an integrated fluorescence tomography system wherein frequency domain fluorescence measurements made on a phantom in area-illumination and area-detection mode were used as inputs to an adaptive finite element-based tomography algorithm to produce three dimensional images of fluorescent targets buried at depths of 1–2 cm from the illumination surface. The increased resolution of our algorithm in conjunction with lower computational costs, as well as the application of reconstruction algorithms to actual measurement data are the main novel points of this paper.

The outline of this article is as follows: in Sec. II, we describe the tissue phantom along with the instrumentation used for acquiring fluorescence emission and excitation source light measurements and the adaptive tomography method used for image reconstruction. Section III details the tomography results obtained for varying depths of fluorescent targets. The impact of adaptivity on the accurate modeling of photon propagation in tissue is illustrated. Finally, Sec. IV details the implications of adaptivity and planar illumination and detection schemes for clinical fluorescence tomography.

II. MATERIALS AND METHODS

Within this section, we describe: (i) the tissue phantom and fluorescent targets used for conducting measurements of fluorescent and excitation light, (ii) the gain modulated image intensified CCD camera system and optical assembly, (iii) the data acquisition procedure for excitation and emission measurements, and (iv) the inverse image reconstruction scheme.

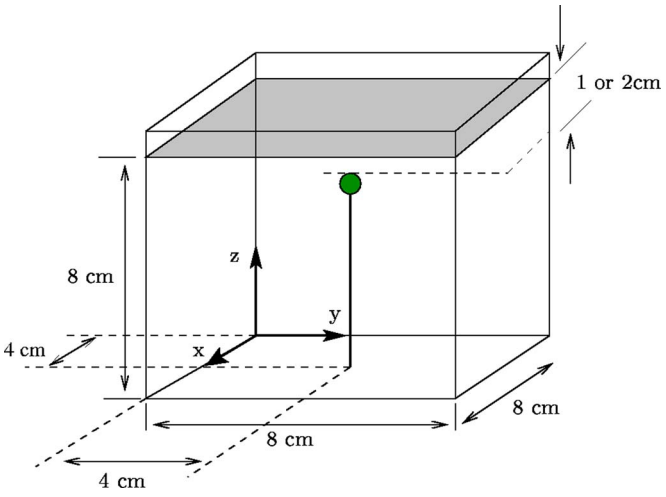

FIG. 1. Tissue phantom with fluorescent target.

A. Tissue phantom

The phantom model consisted of an $8\times8\times8$ cm^3 clear acrylic box filled with 1% Liposyn solution. The fluorescent targets used for this work were blown glass bulbs with an approximate outside diameter of 5 mm and internal diameters of 3–4 mm. The fluorescent targets were filled with 1 μM Indocyanine Green (ICG) solution in 1% Liposyn which was stabilized with the addition of sodium polyaspartate. The excitation and emission wavelengths of ICG were 785 and 830 nm, respectively. The tissue phantom was illuminated at the top surface over a region of approximately 2.5 cm diameter. The targets were fixed on the end of a 1 mm fiber optic attached to the bottom of the box, and positioned at depths of 1 or 2 cm beneath the illumination surface. Figure 1 illustrates the tissue phantom geometry.

In Ref. 18, it was shown that reconstructions from synthetically generated data are also possible for depths slightly larger than 2 cm. Generally, reconstructions are limited by the signal-to-noise ratio that decreases exponentially with depth. We limit our attention to targets no more than 2 cm deep, since this seems to be as far as we can comfortably obtain stable reconstructions with our present experimental setup. Presently ongoing work investigates targets at depths greater than that.

B. Instrumentation

Figure 2 illustrates the homodyne gain modulated image intensified CCD camera system used to acquire frequency domain optical measurements. The tissue phantom was illuminated by a 785 nm laser beam produced by a 70 mW laser diode (Thorlabs, HPD 1105-9mm-D-78505) expanded over an area of approximately 5 cm^2. Measurements were ac-

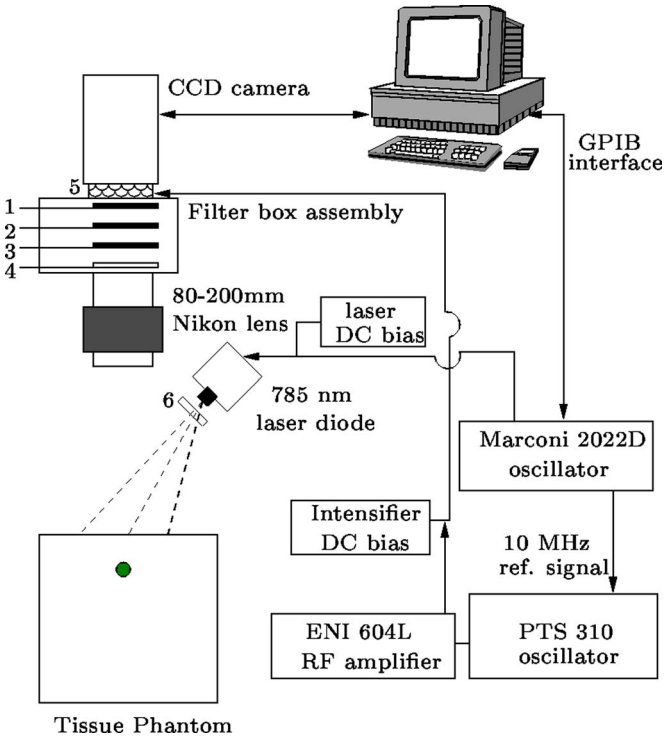

FIG. 2. Instrumentation for acquiring frequency domain fluorescence measurements in a homodyne mode. Numbered components include: 1: neutral density filter (OD-3), 2: 785 nm holographic band rejection filter, 3: 830 nm interference bandpass filter, 4: linear polarizer, 5: image intensifier, and 6: linear polarizer. Optical filters can be moved in and out of the filter box assembly to acquire measurements at excitation and emission wavelengths. Phantom surface image on the CCD camera is expanded to depict measurement data acquisition by raster scanning the CCD pixels.

quired by a 1024×1024 pixel 16-bit frame transfer CCD camera (Photometrics Ltd., series AT200, model SI512B, Tucson, AZ) which was coupled to an image intensifier (ITT Industries Night Vision, model FS9910C, Roanoke, VA). The fluorescence measurements were isolated from the reflected light using a 785 nm holographic band rejection filter (Kaiser Optical Systems Inc., Ann Arbor, MI, model HNPF-75.0-2.0) and an 830 nm interference bandpass filter (Image Quality, Andover Corp., Salem, NH, model 830.0-2.0). Optical filters were contained in a filter box assembly attached to the intensified CCD camera. Sliding trays carried the filters in and out of the light path to enable measuring excitation and fluorescence emission light separately. A 80–200 mm Nikon zoom lens focused the top surface of the phantom onto the image intensifier. The field of view on the phantom surface was a 4 cm diameter circle, with area illumination contained to this region. The pixels on the CCD camera image are treated as individual photon detector locations and excitation and fluorescence emission measurement data are collected by raster scanning across the CCD array.

Frequency domain data were acquired by using the homodyne procedure, wherein the laser diode and the image intensifier are both modulated at 100 MHz by two phase-locked oscillators with a constant phase offset. A PTS-310 frequency synthesizer (Programmed Test Sources Inc., Littleton, MA, model 310M201GYX-53) modulated the photocathode of the image intensifier, and a Marconi signal generator (Marconi Instruments Ltd., Hertfordshire, England, model 2022D) modulated the laser diode. The oscillators were phase locked with a 10 MHz reference signal. In the homodyne mode of data acquisition, the phase of the image intensifier modulation was offset relative to the phase of the laser diode modulation in 32 steps to cover the full 2π cycle, and phase five images were acquired for every phase offset. For each pixel, a sine curve was fitted to these 32×5 data points with a fast Fourier transform and amplitude and phase signal were extracted. See Reynolds *et al.*[19] for a more detailed description of the multipixel frequency domain data acquisition instrumentation.

C. Data acquisition procedure

The instrumentation described in the previous section was used to obtain the frequency domain measurements at excitation and emission wavelengths by changing the optical filters and varying the parameters governing the CCD camera and image intensifier operation.

1. Excitation source characterization

The excitation source was produced by expanding the beam from the laser diode, resulting in a spatially varying distribution of amplitude and phase of the incident excitation light on the phantom surface. This source distribution needs to be determined for successful reconstruction in the inverse imaging algorithm. For excitation measurements, the aperture of the focusing Nikon lens was minimized and the gain on the image intensifier was reduced to avoid saturating the CCD camera. A neutral density filter (OD 3) was also used to further reduce the intensity of excitation light. The integration time was kept at 40 ms. The singly scattered, polarization conserving excitation light signal from the phantom surface was considered to be representative of the incident light. This component was isolated by utilizing two high efficiency (extinction ratio 10 000:1) cross polarizers (Newport Corp., model 05P109AR.16, Irvine, CA). The polarizers were positioned at the laser diode output and image intensifier input. Multiple scattering causes the polarization to be randomized. One set of 32 phase dependent images was acquired with polarizers oriented in parallel. This set of images consisted primarily of the singly scattered component, with a small contribution from multiply scattered light. By subtracting the images acquired by orienting the polarizers in perpendicular direction from those acquired in the parallel direction, the singly scattered component was isolated. The incident excitation source amplitude and phase was determined by performing the fast Fourier transform on the difference images. For more details on the excitation source characterization, see Thompson *et al.*[20,21]

2. Fluorescence emission measurements

For acquiring the fluorescence emission measurements, the signal intensity was increased by maximizing the aperture of the Nikon lens focusing the image of the phantom

surface onto the image intensifier and increasing the gain voltage of the microchannel plate of the image intensifier. The CCD camera images were binned down to 128×128 pixel and the image integration time was kept at 1200 ms. The fluorescence amplitude and phase at each pixel was then computed by the homodyne data processing procedure detailed in the previous section. These measurements were performed for fluorescent target depths of 1 and 2 cm.

D. Inverse imaging scheme

Fluorescence optical tomography is typically performed in a model-based framework wherein a photon transport model in tissue is used to generate predicted boundary fluorescence measurements for a given fluorescence absorption map. The map of the absorption owing to fluorophore is then iteratively updated until the predicted boundary fluorescence measurements converge to the actual experimentally observed fluorescence measurements. For photon propagation in large tissue volumes, the following set of coupled photon diffusion equations are an accurate model

$$-\nabla \cdot [D_x(\mathbf{r})\nabla u(\mathbf{r},\omega)] + k_x u(\mathbf{r},\omega) = 0, \tag{1}$$

$$-\nabla \cdot [D_m(\mathbf{r})\nabla v(\mathbf{r},\omega)] + k_m v(\mathbf{r},\omega) = b_{xm} u(\mathbf{r},\omega). \tag{2}$$

Here,

$$D_{x,m} = \frac{1}{3(\mu_{ax,mi} + \mu_{ax,mf} + \mu'_{sx,m})},$$

$$k_{x,m} = \frac{i\omega}{c} + \mu_{ax,mi}(\mathbf{r}) + \mu_{ax,mf}(\mathbf{r}),$$

$$b_{xm} = \frac{\phi \mu_{axf}}{1 - i\omega\tau(\mathbf{r})},$$

and subscripts x and m denote the excitation and the emission light fields, respectively. u, v are the complex-valued photon fluence fields at excitation and emission wavelengths, respectively; $D_{x,m}$ are the photon diffusion coefficients; $\mu_{ax,mi}$ is the absorption coefficient due to endogenous chromophores; $\mu_{ax,mf}$ is the absorption coefficient due to exogenous fluorophore; $\mu'_{sx,m}$ is the reduced scattering coefficient; ω is the modulation frequency; ϕ is the quantum efficiency of the fluorophore; and finally, τ is the fluorophore lifetime associated with first order fluorescence decay kinetics. These equations are complemented by Robin-type boundary conditions on the boundary $\partial\Omega$ of the domain Ω modeling the near-infrared excitation source

$$\begin{aligned} 2D_x \frac{\partial u}{\partial n} + \gamma u + S(\mathbf{r}) = 0, \\ 2D_m \frac{\partial v}{\partial n} + \gamma v = 0, \end{aligned} \tag{3}$$

where n denotes the outward normal to the surface and γ is a constant depending on the optical reflective index mismatch at the boundary.[22] The complex-valued function $S(\mathbf{r})$ is the excitation boundary source. There is no source term for the emission boundary condition. The goal of fluorescence tomography is to reconstruct the spatial map of coefficients $\mu_{axf}(\mathbf{r})$ and/or $\tau(\mathbf{r})$ from measurements of the complex emission fluence v on the boundary. In this work, we will focus on the recovery of only $\mu_{axf}(\mathbf{r})$. For notational brevity, we set $q = \mu_{axf}$ in the following paragraphs.

We have previously proposed a novel fluorescence tomography algorithm utilizing adaptive finite element methods.[18] In the following, we briefly describe the formulation of the scheme and its application to image reconstructions from experimentally obtained fluorescent measurements on the tissue phantom.

The fluorescence image reconstruction problem is posed as a constrained optimization problem wherein an L_2 norm based error functional of the distance between boundary fluorescence measurements z and the diffusion model predictions v is minimized by variation of the parameter q, with the additional constraint that the coupled diffusion model is satisfied. In a function space setting this minimization problem reads as

$$\min_{q,u,v} J(q,v) \quad \text{subject to} \quad A(q;[u,v])([\zeta,\xi]) = 0. \tag{4}$$

Here, the error functional $J(q,v)$ incorporates a least square error term over the measurement part Σ of the boundary $\partial\Omega$ and a Tikhonov regularization term

$$J(q,v) = \tfrac{1}{2}\|v - \sigma z\|^2_\Sigma + \beta r(q), \tag{5}$$

where $[u,v]$ represent the excitation and emission fluence; $q = \mu_{axf}$ denotes the unknown fluorescence map; and σ is a scaling factor accounting for the unknown excitation source amplitude magnitude. For our instrumentation setup, σ was empirically determined to be 10^{-7}. β is the Tikhonov regularization parameter. The constraint $A(q;[u,v])([\zeta,\xi]) = 0$ is the weak or variational form of the coupled photon diffusion equations in frequency domain with partial current boundary conditions. We obtain it by multiplying the two equations (1)–(2) with the complex conjugate of test functions ζ, $\xi \in H^1(\Omega)$, integrating over the entire domain Ω, and integrating second derivatives by parts

$$\begin{aligned} A(q;[u,v])([\zeta,\xi]) = {} & (D_x \nabla u, \nabla\zeta)_\Omega + (k_x u, \zeta)_\Omega + \frac{\gamma}{2}(u,\zeta)_{\partial\Omega} \\ & + \tfrac{1}{2}(S,\zeta)_{\partial\Omega} + (D_m \nabla v, \nabla\xi)_\Omega \\ & + (k_m v, \xi)_\Omega + \frac{\gamma}{2}(v,\xi)_{\partial\Omega} - (b_{xm} u, \xi)_\Omega. \end{aligned} \tag{6}$$

Here, the inner product is defined as $(f,g)_\Omega = \int_\Omega f(x)\overline{g(x)}dx$, where a bar denotes the complex conjugate. The surface product $(f,g)_{\partial\Omega}$ is similarly defined. This weak form is the basis for our finite element approach[23] to the numerical solution of this equation.

As is well known from optimization theory,[24] a solution of minimization problem (4) can be determined as the stationary point of the Lagrangian

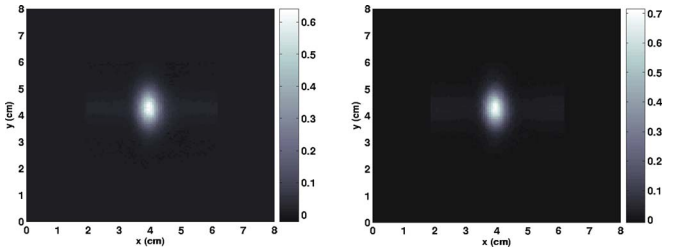

FIG. 3. Excitation source fluence: real (left image) and imaginary (right image) components.

$$L(x) = J(q,v) + A(q;[u,v])([\lambda^{ex},\lambda^{em}]). \tag{7}$$

Here, λ^{ex}, λ^{em} are the Lagrange multipliers corresponding to the excitation and emission diffusion equation constraints, respectively, and we have introduced the abbreviation $x = \{u, v, \lambda^{ex}, \lambda^{em}, q\}$ for simplicity. (If the optimization problem has multiple local minima, each of them will correspond to a stationary point of the Lagrangian. Our algorithms are not able to deal with this situation and will converge to one of the local minima close to the starting point. However, our use of a regularization functional and the fact that we choose β fairly large in the initial steps reduces the chance of getting trapped in a local minimum.)

The stationary point of $L(x)$ is found using the Gauss-Newton method wherein the update direction $\delta x_k = \{\delta u_k, \delta v_k, \delta\lambda_k^{ex}, \delta\lambda_k^{em}, \delta q_k\}$ is determined by solving the linear system

$$L_{xx}(x_k)(\delta x_k, y) = -L_x(x_k)(y) \quad \forall\, y, \tag{8}$$

where $L_{xx}(x_k)$ is the Gauss-Newton approximation to the Hessian matrix of second derivatives of L at point x_k, and y denotes the possible test functions. These equations represent one condition for each variable in δx_k. Once the search direction is computed from Eq. (8), the actual update is determined by calculating a safeguarded step length α_k:

$$x_{k+1} = x_k + \alpha_k \delta x_k. \tag{9}$$

The step-length α_k can be computed from one of several methods, such as the Goldstein-Armijo backtracking line search.[25,26]

The Tikhonov regularization term $\beta r(q)$ added to the minimization functional $J(q,v)$ defined in Eq. (5) is used to control undesirable components in the map $q(\mathbf{r})$ that result from a lack of resolvability. In this contribution, we use the L^2 norm $r(q) = 1/2\|q\|^2$ to penalize large values that would typically occur far from the illumination surface if no regularization was used, since the values of q in these parts of the domain do not significantly affect the predicted fluence v. Other possible choices for $r(q)$ would penalize the variation ∇q instead of the magnitude q of the map to enforce smoothness of the reconstruction. However, since we are looking for a localized target, this would lead to a washed-out reconstruction.

The regularization parameter β is initially set to 10^{-12} and is reduced whenever the misfit $1/2\|v - \sigma z\|^2$ comes to within a factor of 3 of $\beta/2\|q\|^2$. Using this strategy, the regularization term is always present, but never dominates the misfit. Iterations can therefore be considered to reduce the misfit under the constraint that the regularization term stays bounded, rather than attempting to merely reducing the regularization term when the misfit is already small. Note that the form of misfit and regularization terms involving integrals ensures that the values of these functionals do not depend on the chosen discretization, and are robust against mesh refinement that increases the number of unknowns.

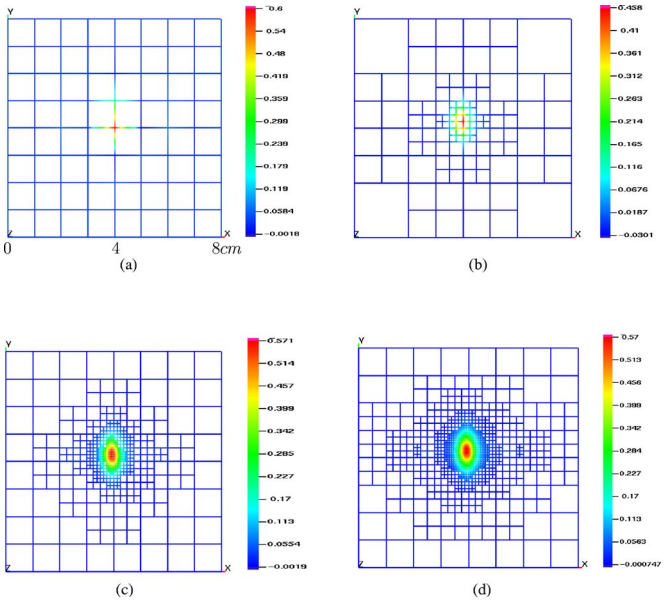

FIG. 4. Forward mesh evolution on the illumination surface. Meshes after (a) 0, (b) 2, (c) 4, and (d) 5 adaptive refinements are depicted.

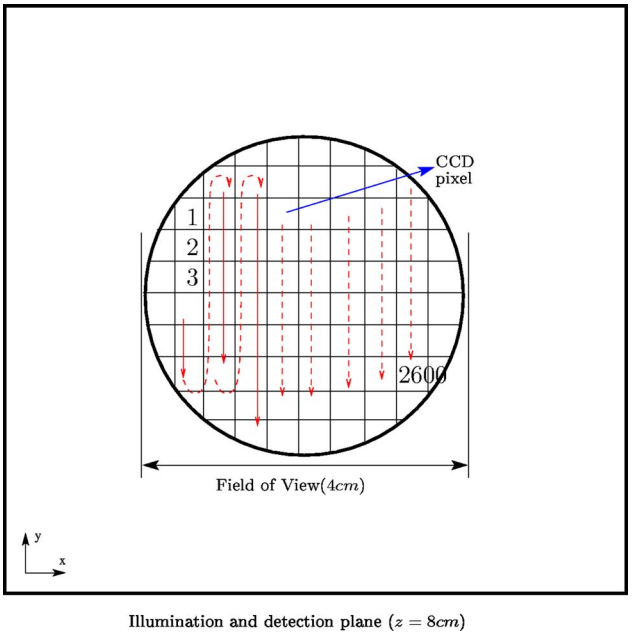

FIG. 5. Raster scanning of the CCD camera pixels is performed to extract the fluorescence measurements on the detection plane. Field of view of the camera system is 4 cm. Pixels in the field of view are numbered and treated as individual detector locations.

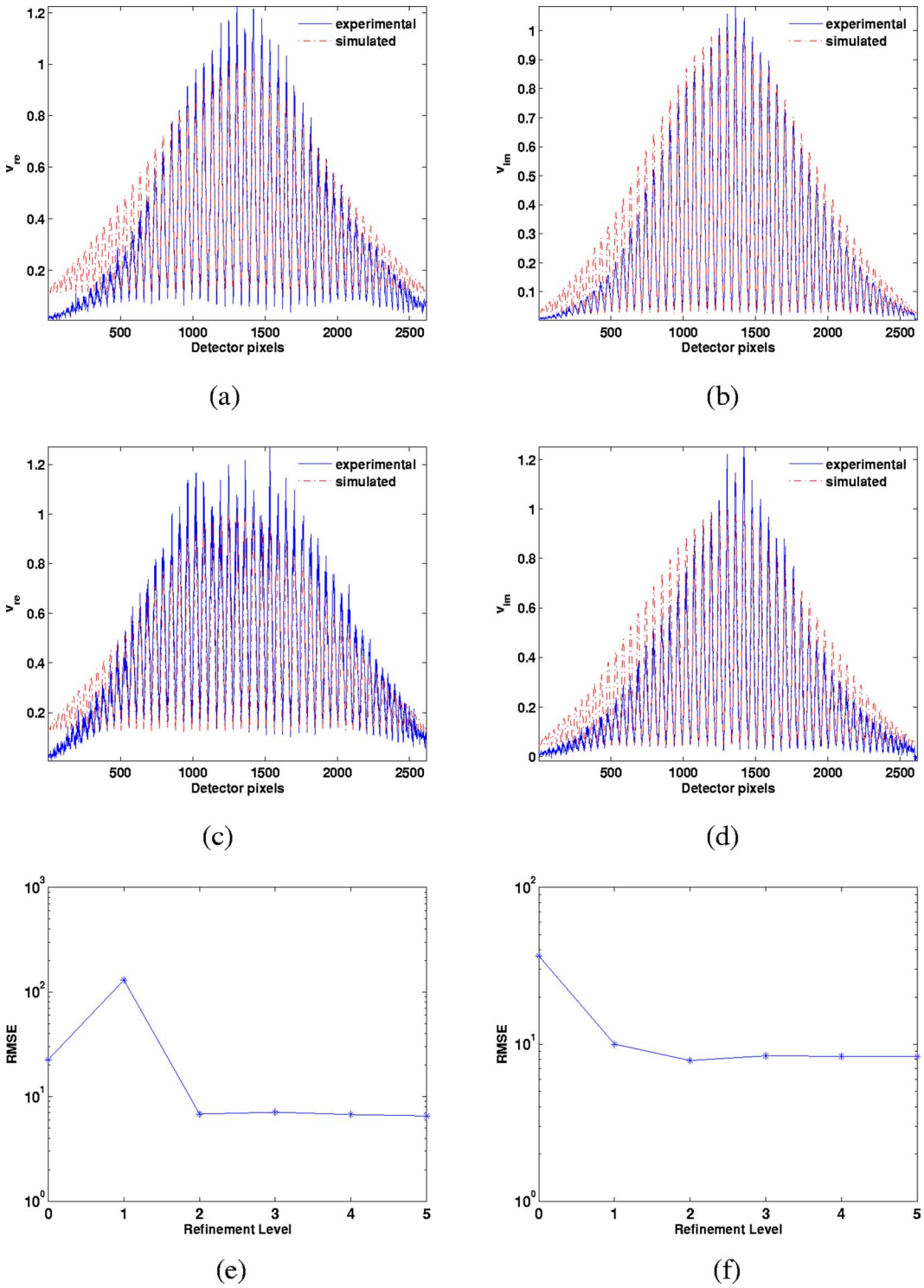

FIG. 6. Experimentally observed and simulated real and imaginary components of fluorescence fluence $\mathrm{Re}(v), \mathrm{Im}(v)$ at the measurement surface, plotted against CCD detector points for (a) and (b) target depths of 1 cm, and (c) and (d) 2 cm. In (e) and (f) we plot the RMSE defined in (10) for a sequence of adaptively refined meshes used for solution of coupled diffusion equations, for target depths of 1 and 2 cm.

For carrying out actual computations, we discretize the Gauss-Newton equations with the finite element method. State and adjoint variables $u, v, \lambda^{\mathrm{ex}}$, and λ^{em} are discretized and solved for on a mesh with continuous finite elements, while the unknown parameter map q is discretized on a separate mesh with discontinuous finite elements. At the end of each Gauss-Newton iteration, we compute a criterion that indicates how far away from the solution we still are. Since we know that at the stationary point is characterized by $L_x(x)=0$, we use the norm of the residual, $\|L_x(x_k)\|$, for this criterion. The computation of this norm is somewhat involved, and we refer the reader to Ref. 26 for more details.

Whenever iterations on this set of meshes have reduced the norm of the residual by a factor of 10^{-3} or the Gauss-Newton step length returned by the line search algorithm has fallen below 0.15, both meshes are refined using *a posteriori* refinement criteria. In this work, the state and adjoint mesh is refined using a variation of the refinement criterion first derived by Kelly *et al.*[27] The mesh for q is refined by computing, for each cell, a discrete approximation to the gradient of q, weighted by the local mesh width[26] and refining the cells with maximum variation in gradient. For both meshes, each cell is refined or coarsened at most once per iteration.

The choice of two separate meshes means that the first mesh can be fine close to the source where the excitation fluence greatly varies, while the second mesh will only be fine close to the fluorescent target and coarse everywhere else. The mesh refinement criteria and actual implementation of the reconstruction algorithm are described in Refs. 18 and 28. The algorithm described above was implemented in a program based on the Open Source deal.II finite element library.[29]

III. RESULTS AND DISCUSSION

A. Excitation source extraction and forward simulation

Conventional optical tomography schemes usually employ fiber optic based source, which are easily simulated in finite element codes as point sources. In the only previous work reported on area-illumination,[14] the expanded area source was modeled as a distribution of point sources. To accurately simulate the expanded source with a collection of point source, Roy *et al.* constructed a finite element mesh which matched with resolution of the CCD pixel array (128×128 nodes) on the top surface of the phantom and had a coarse resolution elsewhere in the phantom. However, this kind of approach is problem dependent and a change in excitation source, will require the manual generation of a new finite element mesh. In contrast, adaptive mesh refinement generates suitable finite element meshes for arbitrary excitation sources from an initial uniform coarse mesh. Figure 3 illustrates the real and imaginary parts of the complex excitation source isolated by utilizing cross polarizers. Since we have to estimate the exact source strength anyway using the factor σ in Eq. (5), we normalize the excitation source to a maximum amplitude of 1. This source is used as input $S(\mathbf{r})$ to the finite element simulation of the coupled diffusion equations for forward and inverse modeling of fluorescence light propagation and generation in the tissue phantom. Figure 4 shows the mesh evolution at the illuminated phantom surface in subsequent refinement steps, demonstrating the way our mesh generation algorithm aids in obtaining finite element discretizations that are extremely well adapted to the requirements of this problem. The simulation is started with coarse cells of 1 cm length, and after five adaptive refinements steps the mesh reflects the structure of expanded laser source.

B. Measurements and model match

As described in Secs. II B and II C, complex fluorescence measurements were acquired for fluorescent targets placed at depths of 1 and 2 cm from the illumination surface. The simulated measurements should agree with experimentally observed fluorescence measurements to a reasonable degree for model based tomography approaches to work. Hence, to validate the experimental measurements, simulated fluorescence predictions were obtained from an adaptive finite element solution of the coupled diffusion equations (1) and (2) for the experimental tissue phantom and fluorescent target geometry. The simulated and observed fluorescence fluence is plotted against the detector points resulting from a raster scan across CCD camera pixels mapping the measurement region. The raster scanning of CCD pixels is illustrated in Fig. 5. Approximately 2600 detector points are obtained within the CCD camera field of view. To account for the different orders of magnitudes of the observed and simulated measurements, the real and imaginary components of the fluorescence measurements were referenced with the detection point with maximum simulated fluorescence value. Figures 6(a)–6(d) show a comparison of real and imaginary parts between experimentally observed and simulated fluorescence υ at the measurement surface for target depths of 1 and 2 cm. As can be seen, observed and simulated fluorescence follow the same general trend; the differences in their profiles are mainly attributed to three reasons: (i) for the purposes of simulation, fluorescent targets were treated as spheres with radius 2.5 mm, however, the actual fluorescent targets were made in a glass blowing workshop and had ellipsoidal shape with varying glass wall thickness; (ii) the image intensifier employed for making measurements had variations in sensitivity across its surface which results in a positive bias for points towards the center of the measurement region; and (iii) measurement data is also corrupted by arbitrary thermal and electronic noise in the gain modulated homodyne instrumentation.

The accuracy of forward simulation of coupled diffusion equations also affects the model mismatch error between the simulated and predicted measurements. To estimate this effect, we computed the root mean squared model mismatch error (RMSE) across the surface area Σ on which we can measure fluences for a sequence of adaptively refined finite element meshes used for forward simulation. We define the RMSE as

$$\mathrm{RMSE} = \sqrt{\sum_{d=1}^{M} |\upsilon_d^{\mathrm{meas}} - \upsilon_d^{\mathrm{sim}}|^2}, \tag{10}$$

where $\upsilon_d^{\mathrm{meas}}$ and $\upsilon_d^{\mathrm{sim}}$ are the measured and simulated complex fluence $\upsilon = \upsilon_{\mathrm{re}} + i\upsilon_{\mathrm{im}}$ at the detection point d, respectively. From Figs. 6(e) and 6(f) it can be seen that the RMSE decreases rapidly during the first couple of iterations of adaptive mesh refinements and then converged to a constant value. This suggest that the numerical error becomes irrelevant after three adaptive mesh refinements, and that on finer meshes the errors in the model, source, and target description

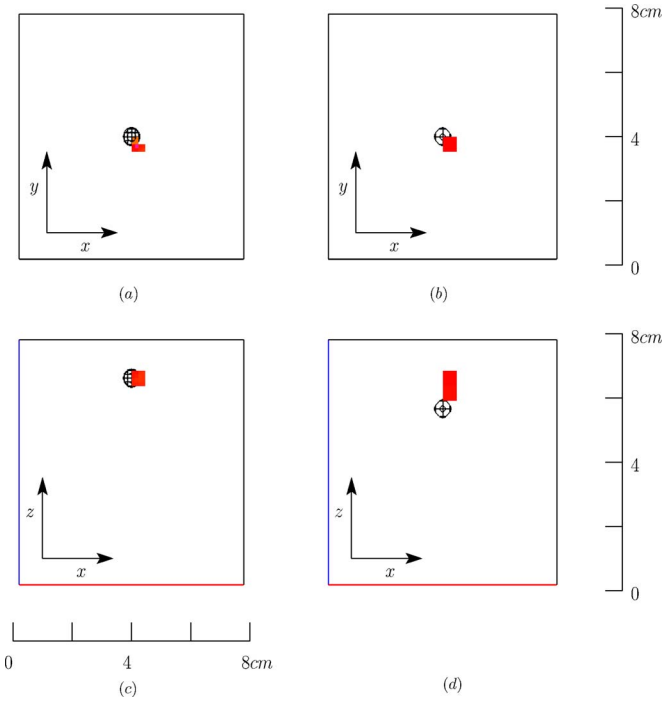

FIG. 7. Reconstructed and true images for 1 and 2 cm deep fluorescent targets are presented. True targets are depicted by the black wireframe, while the reconstructed targets are represented by colored blocks. The top 10% of the contour levels of reconstructed fluorophore distribution are depicted. (a),(b) True and recovered targets (x-y plane view); (c),(d) true and recovered target (x-z plane view). Left column depicts the 1 cm deep target case, while the right column represents the 2 cm deep target.

are the dominant factors in mismatch between numerical prediction and actual measurement.

C. Image reconstructions

The adaptive tomography algorithm described in Sec. II D was used to reconstruct the three dimensional images of fluorescence absorption distribution in the tissue phantom from experimentally observed fluorescence measurements. The image reconstruction procedure was initiated with coarse state ($8\times8\times8=512$ cells) and parameter ($4\times4\times4=64$ cells) meshes. Computations were performed on a 2 GHz Pentium-M notebook computer with 2 GB of memory. Image reconstructions required 12–15 min of computational time depending upon the target depth. Figure 7 depicts the true and reconstructed fluorescent targets for target depths of 1 and 2 cm, where we consider those cells with the top 10% of the contour levels of the reconstructed fluorescence absorption as a fluorescent heterogeneity. Both the state and parameter meshes were automatically refined during the reconstruction process. As shown in Fig. 4, the state mesh was primarily refined at the illumination surface to resolve the expanded laser source, while the parameter mesh was fine mostly in the region containing the recovered fluorescent target (see Fig. 8). Figure 8 also depicts the evolution of the parameter mesh with the Gauss-Newton iterations. The recovered target volume was over-predicted for both 1 and 2 cm deep targets. However, the definition of recovered target volume depended on the arbitrary definition of recovered fluorescent target as the top 10% of contour levels. For the 2 cm deep case, the recovered target was lifted towards the illumination surface. This can be attributed to the lower fluorescence signal penetrating up to the measurement surface, and its greater corruption by excitation light leakage through the fluorescence filters[30,31] than in the case of a 1 cm deep target. The lateral displacement of the recovered targets compared to the true position also occurs due to the uncertainty in positioning of the fluorescent target in the tissue phantom.

Figures 9(a) and 9(b) depict the change in the objective function $J(q,v)$, defined in Eq. (5), with Gauss-Newton iterations. Traditional optical tomography schemes usually show a monotonous decrease in model misfit with the progress of iterations. In contrast, the constrained scheme explained above allows for a violation of the partial differential constraint in favor of a reduction in the objective function, and only exactly satisfies the PDE in the limit of iterations going to infinity; the result is that in our reconstructions, the objective function initially drops very sharply, but may then increase again as the PDE is satisfied better and better. Although the objective function gets minimized in the initial few iterations, Fig. 8 suggests that images continue to improve with succeeding Gauss-Newton iterations on finer meshes.

A better measure of progress is to look at the residual of the optimality conditions $L_x(x_k)$. This residual has two components: the gradient of the objective function (tangential to the solution manifold) and the violations of the diffusion equation and its adjoint; at the solution of the inverse problem, each of these parts should be zero. Unfortunately, mathematically speaking, the residual is an H^{-1} function, and its norm cannot be computed exactly. However, on a given mesh, we can approximate it (for details, see Ref. 26), using the present finite element space. In our algorithm, we choose the step length α_k such that this approximate norm of the residual decreases in each step. The result is shown in Figs. 9(c) and 9(d), where it can be seen that on each mesh, the approximate norm of the residual decreases in each step, even though it seems as if the objective function does not change at all. In these cases, the computed fluences simply moved so that they satisfy the diffusion equation better. The figure also shows how mesh refinement is triggered whenever the residual has been reduced sufficiently, or when a stall is detected. Note that due to the way we compute the approximate norm, no comparison is possible between the residuals on different meshes, and the shown increases upon mesh refinement do not indicate a deterioration of the solution.

Finally, iterations were terminated when the number of Gauss-Newton iterations exceeded 40 or when the algorithm stopped further progress without triggering mesh refinements leading to computer memory saturation. The image reconstruction details are summarized in Table I. The maximum contour level in the reconstructed images of absorption due to fluorophore (μ_{axf}^R) is reported in Table I. The recovered fluorescence absorption coefficient $q\equiv\mu_{axf}$ in both the 1 and

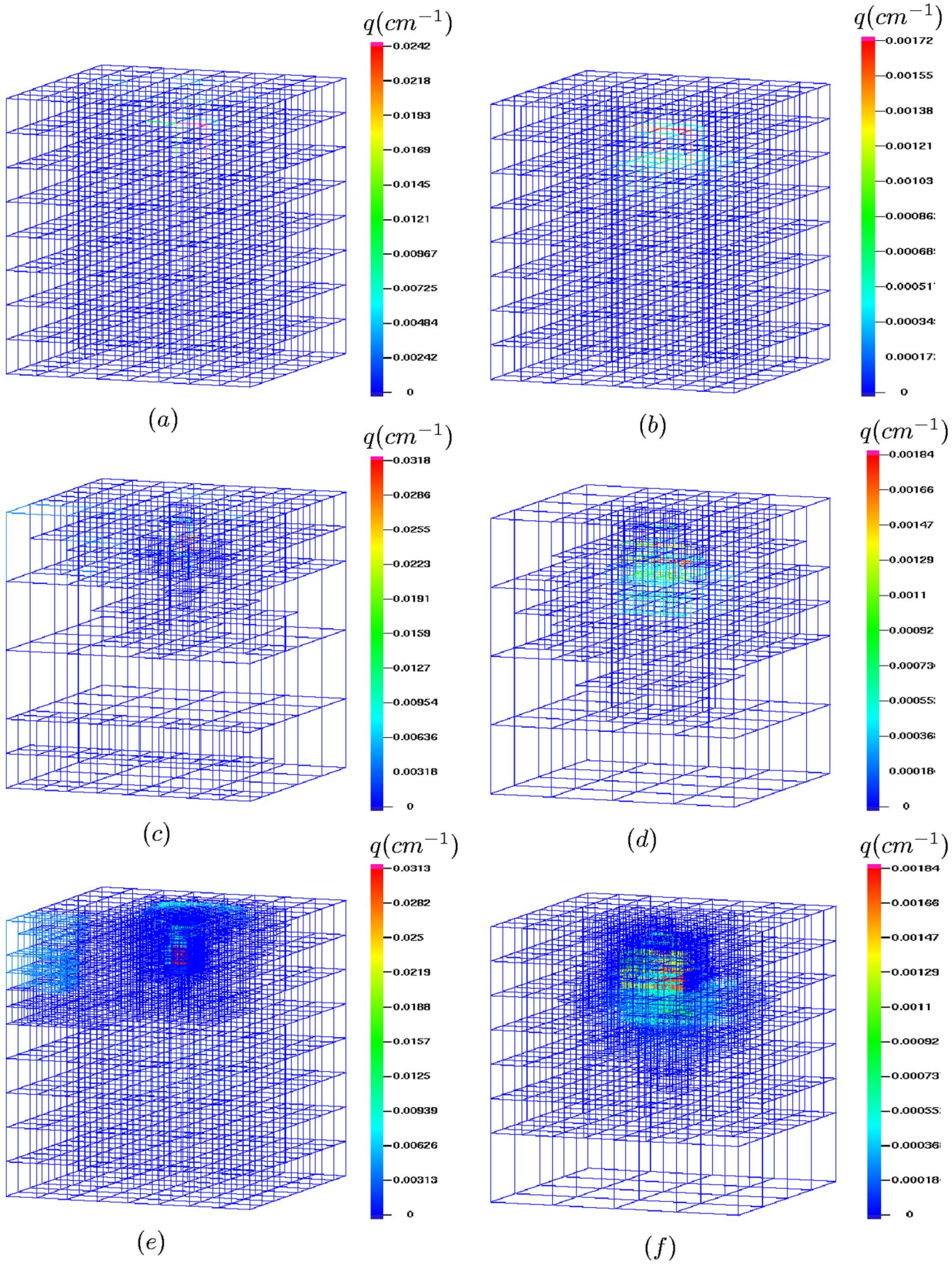

FIG. 8. Parameter mesh adaptation for: 1 cm deep fluorescent target [(a) (c) (e)], (b) 2 cm deep target [(b) (d) (f)]. Top row [(a) (b)] depicts the solutions obtained on the initial coarse mesh; middle row [(c) (d)] depicts the solutions obtained on the mesh after one adaptive refinement; bottom row [(e) (f)] depicts the solutions obtained on the final (5th) adaptively refined mesh.

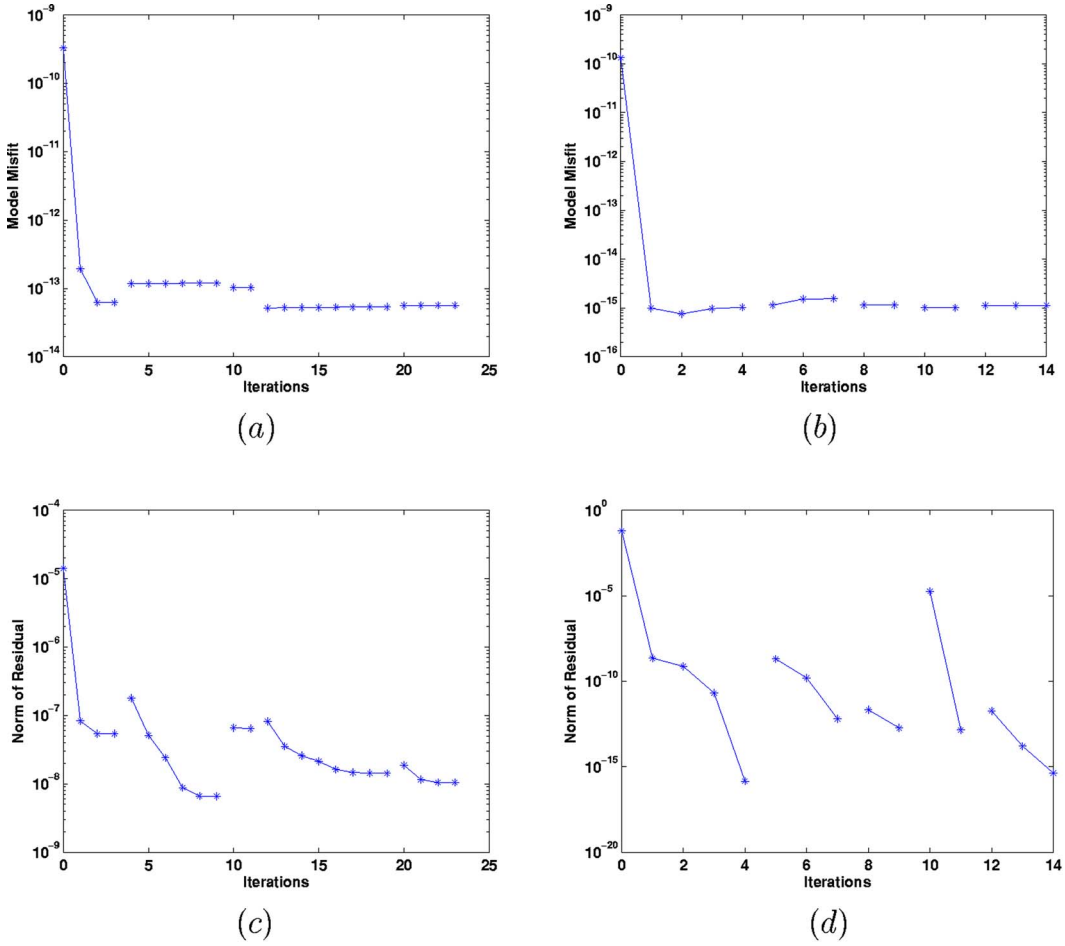

FIG. 9. Top row: Reduction of the objective function $J(q,v)$ with Gauss-Newton iterations. Bottom row: Behavior of the norm of the residual as a function of iterations. Parts (a) and (c) correspond to the 1 cm deep fluorescent target, parts (b) and (d) to the 2 cm deep target. The lines are broken whenever mesh refinement occurs between two iterations.

2 cm targets is underpredicted compared to the actual value of 0.2 cm^{-1}. This effect is common in diffuse optical tomography and results from the nonlinearity of the inverse problem and smoothing effect caused by Tikhonov regularization.

IV. CONCLUSIONS

We have demonstrated a novel and clinically relevant, noncontact fluorescent optical tomography system. Area illumination and area detection frequency domain fluorescence measurements were performed on a 512 ml tissue phantom with a gain modulated image intensified CCD camera operated in a homodyne mode. Fluorescent targets buried at depths of 1 and 2 cm were identified and located successfully by employing a dual mesh adaptive finite element based tomography algorithm. Independent finite element meshes were used for modeling the light propagation in tissue and for iteratively updating the unknown fluorescence absorption map. This allowed for both the efficient numerical simulation of light propagation in tissue as well as the efficient discretization of the fluorescent yield map. In particular, we note that the adaptation of meshes was entirely guided by the results of previous iterations (through the use of *a posteriori*

TABLE I. Summary of the reconstructed images for the 1 and 2 cm deep fluorescent targets. "No. iterations" denotes the number of Gauss-Newton iterations; $1/2\|v-\sigma z\|^2_{\Sigma}$ the final misfit between prediction v and scaled observation z; $(x,y,z)_{\text{true}}$ and $(x,y,z)_{\text{recovered}}$ indicate the centroids of the true and recovered targets; N_q is the number of parameter unknowns in the final parameter mesh; μ^R_{axf} is the recovered fluorescence absorption coefficient in the targets.

Depth (cm)	No. iterations	$1/2\|v-\sigma z\|^2_{\Sigma}$	$(x,y,z)_{\text{true}}$	$(x,y,z)_{\text{recovered}}$	N_q	$\mu^R_{axf}(\text{cm}^{-1})$
1.0	24	7.831×10^{-14}	(4.0,4.0,6.75)	(4.2,3.75,6.75)	2584	0.0282
2.0	14	1.124×10^{-15}	(4.0,4.0,5.75)	(4.25,3.75,6.5)	2416	0.00184

error indicators), instead of *a priori* information as employed in other dual mesh schemes used in optical tomography where data such as from ultrasound imaging[32] are used to generate finite element meshes for unknown optical parameters. Our scheme therefore allows the generation of excellent finite element meshes, which accurately capture the variation in optical properties of tissue, independently of the availability of prior knowledge about the tissue composition. In the examples shown above, the final number of unknown parameters was 2584 and 2416 for the two cases with 1 and 2 cm deep targets. These numbers are an order of magnitude less than the number of unknowns needed by conventional fluorescence tomography schemes[14] for identifying the fluorescence absorption map in the 512 ml tissue phantom, even though the adaptive scheme allowed a finer mesh in the vicinity of the target. The mesh employed by Roy *et al.*[14] for identifying a 1 cm^3 target at a depth of 1 cm had 33 431 unknowns. The reduced number of unknowns in the adaptive scheme, does not only accelerate the solution process, but also acts as a type of additional regularization and allows stable reconstructions in the presence of measurement noise. Further, as Roy *et al.* used only one finite element mesh for solving both the forward and inverse problems, they were forced to construct a specialized finite element to model the area excitation source.

In its present form, the proposed tomography system was limited by two factors: (i) A limited field of view of diameter 4 cm and (ii) low sensitivity of the image intensifier to the large dynamic range of fluorescence intensities over the tissue surface. These limitations affected the accuracy of the recovered location and size of 2 cm deep fluorescent target and prevented the exploration of target depths greater than 2 cm. Improvements in optical design and image intensification should enable fluorescence measurement acquisition over the entire tissue phantom surface, enhance the sensitivity of the fluorescence measurements from targets deeper than 2 cm, and these will be the focus of future work. In Ref. 18, we demonstrated image reconstructions for two fluorescent targets separated by upto 0.16 cm. Attaining comparable resolution in experimental fluorescence optical tomography will depend upon improvements in signal to noise, and better excitation light rejection by fluorescence bandpass and holographic filters.[31] The phantom employed in the current study was composed of a homogeneous liposyn solution. In clinically relevant situations, tissue heterogeneity needs to be taken into account. In a recent manuscript, researchers at PML have reported the robustness of fluorescence tomography to perturbations in endogenous tissue absorption and scattering.[33] Future work will involve the application of tissue heterogeneity models to better mimic the clinically relevant imaging situations. The study reported in this article was concerned with a perfect uptake of fluorescence contrast agent in the target region. Our work is relevant to sentinel lymph node imaging applications in breast cancer patients, especially when the contrast agents are directly injected into lymphatics. Recent experimental results on fluorescence contrast agent based lymph node mapping in animal models by Frangioni *et al.*[34] augur well for the future applications of the proposed tomography technique.

A further obstacle to clinical application are the curved surfaces of realistic bodies. While we have already shown in Ref. 28 that this does not pose a problem in the numerical algorithm, it is an instrumentation challenge since the camera cannot be focused on a curved surface in its entirety. Multiple cameras might be necessary to achieve this. Optical markers can then be used to characterize the exact shape of the surface, as well as to mitigate the effects of patient movements, see, for example, Ref. 35. Such techniques will obviously also have to be part of future work to make the technology available for clinical settings.

ACKNOWLEDGMENTS

The authors acknowledge the reviewers' careful and knowledge reading of the manuscript. Their comments and suggestions have significantly helped to improve this article. The funding for this research was provided by NIH Grant No. CA R01 112679.

[a]Electronic mail: amitj@bcm.edu

[1]E. E. Graves, J. Ripoll, R. Weissleder, and V. Ntziachristos, "A submillimeter resolution fluorescence molecular imaging system for small animal imaging," Med. Phys. **30**, 901–911 (2003).
[2]E. M. Sevick-Muraca and C. L. Burch, "The origin of phosphorescent and fluorescent signals in tissues," Opt. Lett. **19**, 1928–1930 (1994).
[3]E. M. Sevick-Muraca, G. Lopez, T. L. Troy, J. S. Reynolds, and C. L. Hutchinson, "Fluorescence and absorption contrast mechanisms for biomedical optical imaging using frequency-domain techniques," Photochem. Photobiol. **66**, 55–64 (1997).
[4]X. D. Li, M. A. O'Leary, D. A. Boas, B. Chance, and A. G. Yodh, "Fluorescent diffuse photon density waves in homogenous and heterogeneous turbid media: Analytic solutions and applications," Appl. Opt. **35**, 3746–3758 (1996).
[5]X. D. Li, B. Chance, and A. G. Yodh, "Fluorescent heterogeneities in turbid media: limits for detection, characterization, and comparison with absorption," Appl. Opt. **37**, 6833–6844 (1998).
[6]M. A. O'Leary, D. A. Boas, B. Chance, and A. G. Yodh, "Reradiation and imaging of diffuse photon density waves using fluorescent inhomogeneities," J. Lumin. **60**, 281–286 (1994).
[7]M. A. O'Leary, D. A. Boas, B. Chance, and A. G. Yodh, "Fluorescence lifetime imaging in turbid media," Opt. Lett. **20**, 426–428 (1996).
[8]J. C. Schotland, "Continuous wave diffusion imaging," J. Opt. Soc. Am. A **14**, 275–279 (1997).
[9]V. Chernomordik, D. Hattery, I. Gannot, and A. H. Gandjbakhche, "Inverse method 3-D reconstruction of localized in vivo fluorescence-application to Sjøgren syndrome," IEEE J. Sel. Top. Quantum Electron. **54**, 930–935 (1999).
[10]J. Wu, Y. Wang, L. Perleman, I. Itzkan, R. R. Desai, and M. S. Feld, "Time resolved multichannel imaging of fluorescent objects embedded in turbid media," Opt. Lett. **20**, 489–491 (1995).
[11]E. L. Hull, M. G. Nichols, and T. H. Foster, "Localization of luminescent inhomogeneities in turbid media with spatially resolved measurements of CW diffuse luminescence emittance," Appl. Opt. **37**, 2755–2765 (1998).
[12]A. Milstein, S. Oh, K. J. Webb, C. A. Bouman, Q. Zhang, D. Boas, and R. P. Milane, "Fluorescence optical diffusion tomography," Appl. Opt. **42**, 3061–3094 (2003).
[13]M. J. Eppstein, D. J. Hawrysz, A. Godavarty, and E. M. Sevick-Muraca, "Three dimensional near infrared fluorescence tomography with Bayesian methodologies for image reconstruction from sparse and noisy data sets," Proc. Natl. Acad. Sci. U.S.A. **99**, 9619–9624 (2002).
[14]R. Roy, A. B. Thompson, A. Godavarty, and E. M. Sevick-Muraca, "Tomographic fluorescence imaging in tissue phantoms: A novel reconstruction algorithm and imaging geometry," IEEE Trans. Med. Imaging **24**, 137–154 (2005).

[15]A. Godavarty, M. J. Eppstein, C. Zhang, S. Theru, A. B. Thompson, M. Gurfinkel, and E. M. Sevick-Muraca, "Fluorescence-enhanced optical imaging in large tissue volumes using a gain-modulated ICCD camera," Phys. Med. Biol. **48**, 1701–1720 (2003).
[16]J. Lee and E. M. Sevick-Muraca, "Three-dimensional fluorescence enhanced optical tomography using referenced frequency-domain photon migration measurements at emission and excitation wavelengths," J. Opt. Soc. Am. A **19**, 759–771 (2002).
[17]V. Ntziachristos and R. Weissleder, "Ccd-based scanner for tomography of fluorescent near-infrared probes in turbid media," Med. Phys. **29**, 803–809 (2002).
[18]A. Joshi, W. Bangerth, and E. M. Sevick-Muraca, "Adaptive finite element modeling of optical fluorescence-enhanced tomography," Opt. Express **12**, 5402–5417 (2004).
[19]J. S. Reynolds, T. L. Troy, and E. M. Sevick-Muraca, "Multi-pixel techniques for frequency-domain photon migration imaging," Biotechnol. Prog. **13**, 669–680 (1997).
[20]A. B. Thompson and E. M. Sevick-Muraca, "NIR fluorescence contrast enhanced imaging with ICCD homodyne detection: Measurement precision and accuracy," J. Biomed. Opt. **8**, 111–120 (2002).
[21]S. L. Jacques, J. R. Roman, and K. Lee, "Imaging superficial tissues with polarized light," Lasers Surg. Med. **26**, 119–129 (2000).
[22]A. Godavarty, D. J. Hawrysz, R. Roy, E. M. Sevick-Muraca, and M. J. Eppstein, "Influence of the refractive index-mismatch at the boundaries measured in fluorescence enhanced frequency-domain photon migration imaging," Opt. Express **10**, 650–653 (2002).
[23]S. C. Brenner and L. R. Scott, *The Mathematical Theory of Finite Element Methods* (Springer, Berlin, 2002).
[24]J. Nocedal and S. J. Wright, *Numerical Optimization* (Springer, New York, 1999).
[25]R. Roy and E. M. Sevick-Muraca, "Truncated Newton's optimization schemes for absorption and fluorescence optical tomography: Part(1) theory and formulation," Opt. Express **4**, 353–371 (1999).
[26]W. Bangerth, "Adaptive finite element methods for the identification of distributed coefficients in partial differential equations," Ph.D. thesis, University of Heidelberg, 2002.
[27]D. W. Kelly, J. P. de, S. R. Gago, O. C. Zienkiewicz, and I. Babuška, "*A posteriori* error analysis and adaptive processes in the finite element method: Part I—Error analysis," Int. J. Numer. Methods Eng. **19**, 1593–1619 (1983).
[28]W. Bangerth, A. Joshi, and E. M. Sevick-Muraca, "Adaptive finite element methods for increased resolution in fluorescence optical tomography," Progr. Biomed. Optics Imag. **6**, 318–329 (2005).
[29]W. Bangerth, R. Hartmann, and G. Kanschat, `deal. II` *Differential Equations Analysis Library*, *Technical Reference*, 2006. http://www.dealii.org/.
[30]J. P. Houston, A. B. Thompson, M. Gurfinkel, and E. M. Sevick-Muraca, "Sensitivity and penetration depth of NIR fluorescence contrast enhanced diagnostic imaging," Photochem. Photobiol. **77**, 77–103 (2003).
[31]K. Hwang, J. Houston, J. Rasmussen, A. Joshi, S. Ke, C. Li, and E. M. Sevick-Muraca, "Improved excitation light rejection enhances small animal fluorescent optical imaging," J. Mol. Imaging **4**(3), 194–204 (2005)
[32]M. Huang and Q. Zhu, "Dual-mesh optical tomography reconstruction method with a depth correction that uses a priori ultrasound information," Appl. Opt. **43**, 1654–1662 (2004).
[33]A. Sahu, R. Roy, A. Joshi, and E. M. Sevick-Muraca, "Evaluation of anatomical structure and non-uniform distribution of imaging agent in near-infrared fluorescence-enhanced optical tomography," Opt. Express **13**, 10182–10199 (2005).
[34]S. Kim, Y. T. Lim, E. G. Soltesz, J. Lee, A. M. DeGrand, A. Nakayama, J. A. Parker, T. Mihaljevic, R. G. Laurence, D. M. Dor, L. H. Cohn, M. G. Bawendi, and J. V. Frangioni, "Near-infrared fluorescent type II quantum dots for sentinel lymph node mapping," Nat. Biotechnol. **22**, 93–97 (2004).
[35]M. Schneberger, T. Liebler, and W. Schlegel, "High precision 3d acquisition: Video-based patient positioning and optical tracking," in Proceedings of the 2nd European Medical and Biological Engineering Conference, Vienna, Austria, 2002.